



Highly efficient electrodes for supercapacitors using silver-plated carbon nanofibers with enhanced mechanical flexibility and long-term stability

Yong Il Kim^{a,1}, Edmund Samuel^{a,1}, Bhavana Joshi^a, Min-Woo Kim^a, Tae Gun Kim^a, Mark T. Swihart^b, Sam S. Yoon^{a,*}

^a School of Mechanical Engineering, Korea University, Seoul 136-713, Republic of Korea

^b Department of Chemical & Biological Engineering, University at Buffalo, The State University of New York, Buffalo, NY 14260-4200, USA

HIGHLIGHTS

- Silver-coated freestanding carbon nanofibers were fabricated for supercapacitors.
- Carbon nanofibers encased with silver shells exhibited superior flexibility.
- Good electrical conductivity of silver shell structure led to superior capacitance.
- The core-shell structure ensured long-term stability of the electrode performance.
- Specific capacitance retention after $N = 10,000$ charge-discharge cycles was 100%.

ARTICLE INFO

Keywords:

Electroplating
Electrospinning
Ag
Carbon nanofiber
Flexible electrode
Supercapacitor

ABSTRACT

Highly flexible freestanding carbon nanofibers were electroplated with silver for use in supercapacitor applications. The brittle carbon nanofibers were encased within bendable silver shells to provide superior flexibility and resilience of the supercapacitors. The enhanced electrical conductivity derived from the silver shell structure dramatically increased the capacitance of the supercapacitor. The silver shell also conferred structural stability to the carbon core, thus furnishing stable, long-term electrode performance. Nearly 100% of the specific capacitance was retained after $N = 10,000$ galvanostatic charge-discharge cycles. The mechanical endurance or stability of the fabricated electrode was evaluated using 1,000 bending cycles, demonstrating that the electrode performance remained unchanged. Cyclic voltammetry and galvanostatic discharge curves were measured at various scan rates and current densities. The fabricated electrodes were characterized by scanning electron microscopy, X-ray photoelectron spectroscopy, and transmission electron microscopy, which clearly illustrated the carbon-core and silver-shell structure.

1. Introduction

Supercapacitors (SCs) have been used in hybrid heavy-electrical vehicles and in portable, wearable, and flexible electronic devices. Electrical charge is stored at the electrode-electrolyte interface in supercapacitors [1–3]. In general, high power density, long-term stability, and rapid charge-discharge capability are the measures of supercapacitor performance. In addition, flexibility is required for the use of supercapacitors in wearable and portable electronic devices [4,5]. The requirements of flexibility and long-term stability are the main bottlenecks to greater use of supercapacitors in these devices. Addressing these challenges would expand the use and performance of

supercapacitors.

Carbon-based electrodes have been widely used in supercapacitor electrodes. Carbon delivers excellent electrochemical double layer capacitance (EDLC) while offering good electrical conductivity and long-term stability [6]. However, carbon-based materials (such as graphite, carbon nanotubes, and nanofibers) suffer from low energy density [7]. To increase the energy density, hybrid materials with high electrical conductivity have been developed as composites with carbon [5]. For example, conducting polymers [8] or metal oxides [9] have been used as pseudocapacitive materials to increase the energy density of supercapacitor electrodes. Additionally, carbon materials containing heteroatoms such as silver and nitrogen provide improved electron transfer

* Corresponding author.

E-mail address: skymoon@korea.ac.kr (S.S. Yoon).

¹ These authors have contributed equally.

relative to only carbonaceous material [10]. However, such hybrids generally suffer from electrochemical degradation after repeated cycling, with poor long-term stability [11,12]. Thus, noble metals such as silver, gold, platinum, iridium and palladium, which are less susceptible to degradation, have been used to confer high power density and long-term stability to the electrodes [13–15].

Silver is certainly a good candidate as a complement to carbon. Moon et al. [16] used silver nanowires coated with gold in a transparent and stretchable supercapacitor. Although silver nanowires are nanomaterials that are commonly used in flexible and wearable electronic devices, the silver nanowire network suffers from inherent high contact resistance between nanowires. Nanocomposites of silver nanoparticles with graphene, carbon nanotubes, metal oxides, or conducting polymers have been tested in various energy storage applications [17–19]. When Ag was used with carbon in composite form, no pseudocapacitance was observed. However, it enhanced the EDLC due to larger electrochemical activity. Studies of nanocomposites of Ag/PANI (polyaniline conducting polymer) synthesized by Patil et al. [20] and Tang et al. [21] reported that incorporation of Ag promotes effective charge transfer from PANI through polaron formation. Electroless Ag nanoparticle deposition over stainless steel results in high specific energy due to faster transfer of electrons and access of electrolytes via a porous nanostructure [22]. Silver was also reported to be used with metal oxides including MnO, NiO, CuO, and Co₃O₄. In those cases, the presence of silver alleviates problems associated with the low electrical conductivity of metal oxides [23–26].

A simple electrospinning process can produce a continuous nanofiber, which precludes the issue of high contact resistance of the nanowires; for this reason, nanofibers have merits over nanowires [27]. In addition, carbon nanofibers offer good structural benefits because of their high specific surface area for efficient ion adsorption, good electrical conductivity for efficient charge mobility, and facile control of the pore distribution, which controls the overall ionic diffusion. However, carbon nanofibers are brittle and thus electrodes made from them have limited flexibility. This shortcoming can be circumvented by encasing them in a flexible silver shell, which is achieved by electroplating [28].

Herein, we introduce, for the first time, carbon nanofibers electroplated with silver to improve electrode flexibility in supercapacitors. Because of the high electrical conductivity of silver, the electrode energy density also increased significantly after silver coating. Moreover, the carbon encapsulated in the silver shell should retain stable long-term electrochemical performance while being protected by the silver encasement. Therefore, the carbon-core and silver-shell structure is an ideal nanostructure for simultaneously achieving the trifecta of flexibility, high electrochemical performance, and long-term stability without degradation of the mechanical structure of the carbon nanofibers. A bending cycle test is performed to demonstrate the mechanical stability of the fabricated electrode. The mechanical endurance of the composite at severe bending radii is also demonstrated. Quantitative comparison against existing data from previous relevant studies is presented to highlight the enhanced long-term stability of the core-shell nanofiber electrode.

2. Materials and methods

2.1. Pre-fabrication of carbonized nanofibers

A faint yellow polymer solution of 8 wt% polyacrylonitrile (PAN, $M_w = 150$ kDa, Sigma-Aldrich) was prepared by dissolving 4 g of PAN in 46 g of *N,N*-dimethylformamide (DMF, 99.8%, Sigma-Aldrich) with stirring for 24 h. The polymer solution was then electrospun using two syringes with syringe pumps (Legato 100, KD Scientific Inc.), 18-gauge needles (Nordson EFD), and a high-voltage power supply (EP20P2, Glassman High Voltage Inc.) to prepare the nanofibers (NFs) [29] over a drum collector, as illustrated in Fig. 1a. Electrospinning of the PAN nanofiber was carried out by pumping the solution through the needles

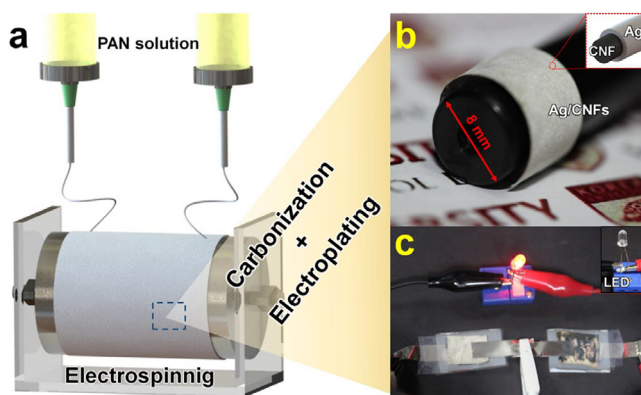


Fig. 1. Schematic of (a) electrospinning setup, (b) flexible Ag/CNF wrapped around 8 mm diameter rod, and (c) photograph of glowing LED powered by two flexible supercapacitors connected in series.

at a flow rate (Q_{es}) of $200 \mu\text{L}\cdot\text{h}^{-1}$ for 90 min. A high DC voltage (V_{es}) of 7.5 kV was applied to the needles to form a stable Taylor cone at the needle tips and successfully form the NFs. A distance of 15 cm between the drum collector and each needle tip was used to generate NF mats with dimensions of $30 \times 15 \text{ cm}^2$. The PAN NF mats were stabilized in air at 280°C for 30 min, after heating at a rate of $5^\circ\text{C}\cdot\text{min}^{-1}$. Further, the samples were carbonized under an argon (Ar) atmosphere at 800°C for 1 h after heating at a rate of $3^\circ\text{C}\cdot\text{min}^{-1}$. Thus, the PAN NFs were converted to carbon nanofibers (CNFs).

2.2. Fabrication of Ag/CNF nanofibers

The silver electroplating solution was prepared by blending 250 mL of KS-700 solution (Poongwon Chemical) with 200 mL of deionized (DI) water (Samchun Pure Chemical) at 45°C . The KS-700 solution consisted of 6% (v/v) of sodium borate ($\text{Na}_2\text{B}_4\text{O}_7$), 79% (v/v) of H_2O , 10% (v/v) of potassium phosphate (KH_2PO_4), and 5% (v/v) of phosphates. A 60 g portion of potassium silver cyanide ($\text{KAg}(\text{CN})_2$, Ag 54%, Poongwon Chemical) was added to the solution, and the total volume of the solution was adjusted to 500 mL with DI water. The temperature of the solution was maintained at 65°C and 100 g of potassium cyanide (KCN, 98%, Poongwon Chemical) was added. The pH of the solution was adjusted to 4.5 using sodium hydroxide (NaOH, 98%, Sigma-Aldrich).

Both sides of the CNF mat were lightly sputtered with platinum (MSP-1S, Vacuum Device Inc.) before the electroplating process. Note that sputtering of a Pt layer a few nm thick on the PAN NFs was sufficient to initiate electroplating by enhancing the electrical conductivity [28]. The Pt-sputtered CNF mat and Pt-coated titanium mesh separated by a distance of 2 cm were then immersed in the Ag-electroplating solution as the cathode and anode, respectively. A DC voltage of $V_{ep} = 8 \text{ V}$ was maintained for 60 s by using a power supply (SPS-1820, GW Instek, Taiwan). The Ag-plated CNF mat was rinsed with DI water for 5 s and dried for several minutes by blowing with Ar to prevent oxidation. The obtained white Ag/CNF fiber (Fig. 1b) was very flexible and suitable for supercapacitor application, as demonstrated by the light emitting diode (LED) glow test presented in Fig. 1c. Two symmetric cells with dimensions of $2 \times 2 \text{ cm}^2$ were prepared using a polymer sheet (550R, 3M) and KOH electrolyte (85%, Sigma-Aldrich) and arranged in series using Ni contacts for this demonstration.

2.3. Characterization

The surface morphologies of the Ag/CNF mats were observed by field-emission scanning electron microscopy coupled with energy-dispersive X-ray spectroscopy (FE-SEM/EDX, Quanta 250 FEG, FEI). The crystallinity and chemical composition of the mats were analyzed by X-ray diffraction (XRD, SmartLab, Rigaku) and X-ray photoelectron

spectroscopy (XPS, X-tool, ULVAC-PHI), respectively. A dual-beam focused ion beam (FIB) system (LVRA3 XMH, TESCAN) was used for Ag/CNF milling for acquisition of cross-sectional images by transmission electron microscopy (TEM, JEM 2100F, JEOL Inc.). Note that in the FIB process, rough cuts were performed with a beam current of 7–15 nA at 30 kV, and final cleaning was conducted with a beam current of 3–7 nA at 30 kV to ensure minimal ion damage. The surface areas of composites were determined from N₂ adsorption and desorption isotherms measured using a volumetric adsorption apparatus (Tristar 3000, Micromeritics). Before N₂ adsorption measurements the sample was pretreated at 70 °C for 48 h under high vacuum (< 10⁻⁶ Torr).

2.4. Electrochemical tests

The freestanding Ag/CNF mats were very flexible and could be used as working electrodes directly after punching, as shown in Fig. 1b and 1c. We punched the mats with a diameter of $D_{\text{elec}} = 14$ mm (total area $A_{\text{elec}} = 1.54$ cm²) and fabricated two-electrode symmetric coin cells (CR2032 type), in which Ag/CNF mats were used for both electrodes. A polymer film (3501 Celgard) was used as a separator between the two electrodes. Aqueous KOH (4, 6, 8M) solutions were used as the electrolyte. For the cyclic voltammetry (CV) measurements, the potential window was set at 0 to 0.6 V, and measurements were performed at different scan rates (10, 50, and 100 mV·s⁻¹). Galvanostatic discharging/charging (GCD) tests were carried out between 0 and 0.6 V. Long-term (LT) cycling tests were conducted at a current density of 0.15 mA·cm⁻².

Two-electrode asymmetric coin cells (with the Ag/CNF composite and CNFs as the two electrodes, CR2032 type) were produced using a method similar to that used for the symmetric cells. We punched Ag/CNF, and CNF mats with diameters of $D_{\text{elec}} = 14$ mm and fabricated a two-electrode asymmetric coin cell, in which the Ag/CNF and CNF mats were used for the respective electrodes. A polymer film (3501 Celgard) was used as a separator and 6M KOH aqueous solution was used as the electrolyte. CV measurements were performed over a potential window of -0.6–0.6 V. The GCD tests were carried out from 0 to 1.2 V, and the difference in each range was used to compare the energy density. Long-term (LT) cycling tests were also conducted at a current density of 0.15 mA·cm⁻².

2.5. Bending test

After evaluating the electrochemical properties of the Ag/CNFs cells, the mechanical reliability during bending was investigated. First, bending was repeated for 1,000 cycles to investigate the mechanical stability of the Ag/CNF mat. For the bending test, a flexible symmetric SC was produced by lamination of a polymer sheet, with two electrodes electrically isolated by a separator and 6M KOH as the aqueous electrolyte. The flexible SC was then bent repetitively around one axis, as shown in the inset of Fig. 7c. The changes in the capacitance as a function of the number of bending cycles were measured in the presence of 6M KOH. The bending radius was maintained at 8 mm.

3. Results and discussion

The surface morphology of the CNFs and CNFs decorated with silver nanoparticles (Ag/CNF) were observed by FE-SEM, as shown in Fig. 2a and b. The surface of the CNFs appeared to be smoother. After Ag-electroplating, the fiber surface became rough and fiber diameter increased due to the Ag nanoparticle coating over the fiber. The average diameters of the CNFs and Ag/CNFs were ~190 and ~390 nm, respectively, illustrating that the voids between the CNFs was reduced after Ag electroplating. Considering the difference between the diameters of the Ag/CNFs and CNFs, the thickness of the Ag shell was estimated as ~100 nm. Further, the interconnected junctions observed for the Ag/CNFs (Fig. 2b) ensured high conductivity of the fibers,

resulting in excellent electrochemical performance, demonstrating that electroplating is viable for the fabrication of such electrodes. [28]

The structure of the Ag deposited on the fiber surface was analyzed by XRD (Fig. 2c). The pattern shows diffraction peaks at $2\theta = 38.0^\circ$, 44.1° , 64.3° , and 77.3° , corresponding to the (1 1 1), (2 0 0), (2 2 0), and (3 1 1) planes of cubic Ag (JCPDS No. 04-0783). The estimated average crystal size of the Ag nanoparticles was ~18.1 nm, as calculated by applying the Scherrer equation. The Ag 3d core XPS spectrum in Fig. 2d shows sharp peaks at 368.1 and 374.3 eV attributed to the Ag 3d_{5/2} and Ag 3d_{3/2} states, respectively. The 3d spin orbit splitting energy of 6.2 eV is consistent with the values previously reported, confirming that Ag exists in its zerovalent metallic form. [30–32] No other peaks were observed, which suggests the absence of other impurities or oxidation states. Thus, the XRD and XPS data confirm that silver was in the metallic state (Ag⁰) in the Ag/CNF composite.

The low-resolution top-view SEM image of the Ag/CNF composite subjected to focused-ion beam milling is presented in Fig. 3a. Further, a cross-section of the sample collected by FIB milling was used for TEM analysis. The selected area electron diffraction (SAED) pattern presented in Fig. 3b shows two clear diffraction rings that can be indexed to the (2 0 0) and (3 1 1) planes of cubic Ag. The low-magnification cross-sectional TEM image of the Ag/CNF sample is presented in Fig. 3c. The CNFs were clearly completely covered with a circular coating of Ag nanoparticles. However, the random growth of the fibers during electrospinning resulted in interconnected junctions. Thus, during the electroplating of Ag, the areas at the junctions showed some morphological deviation. The red circle in Fig. 3c highlights specific fibers that are shown in the high-magnification TEM image presented in Fig. 3d. The cross-sectional view of the Ag/CNF composite demonstrates the core-shell structure, where the core and shell consisted of carbon and Ag, respectively. For the selected fiber, the thickness of the outer Ag and inner C layers were 40 and 85 nm, respectively (Fig. 3e). Elemental mapping (Fig. 3d) confirmed the presence of carbon in the core region and Ag in the shell.

The N₂ adsorption test of CNF and Ag/CNF presented in Fig. S1 clearly shows type IV characteristic curves. The CNF shows hysteresis at very high relative pressure suggesting presence of macro and mesopores. On the other hand, Ag/CNF indicates presence of micropores based on the hysteresis in N₂ adsorption desorption curve at lower relative pressure. The surface area observed by Brunauer-Emmett-Teller (BET) analysis along with pore volume and pore size is presented in Table S1.

Fig. S2a and b show the CV test results of a symmetric CNF supercapacitor coin cell. The cyclic voltammetry test in two different potential window ranges is presented. Over the smaller potential window (0 – 0.6 V) the output current is smaller in comparison to current response when the potential window was increased to 1.2 V (-0.6 to 0.6). Fig. S2c and d shows CV curves of a symmetric CNF/CNF SC cell, a symmetric (Ag/CNF)/(Ag/CNF) cell and an asymmetric CNF/(Ag/CNF) SC cell in two different potential windows. The CNF/(Ag/CNF) SC cell clearly exhibits exceptional charge accumulation at the electrodes much closer to capacitive characteristic curves. Moreover, the peak anodic and cathodic peaks of the asymmetric SC cell with 1.2 V potential window is remarkably larger than its two counterpart symmetric cells. The 1,000 bending cycle test was performed on a CNF symmetric SC cell as presented in Fig. S3 with a bending radius of 8 mm (see also Fig. 7c) As a result, further experiments were conducted on this range. However, due to broken nanofibers (see Fig. S5a and c) of the CNF symmetric SC cell, current decreases slightly after 1,000 bending cycles.

A symmetric coin cell assembled with the Ag/CNF composite and KOH electrolyte of different concentrations (4, 6, and 8M) was used for cyclic voltammetry measurements, as shown in Fig. 4a–c. When the scan rate was increased from 10 to 100 mV·s⁻¹, the area under the curves became larger. The capacitive potential region is the potential range in which the cyclic voltammograms are either rectangular (ideal supercapacitor) or quasi-rectangular (pseudocapacitor) [33];

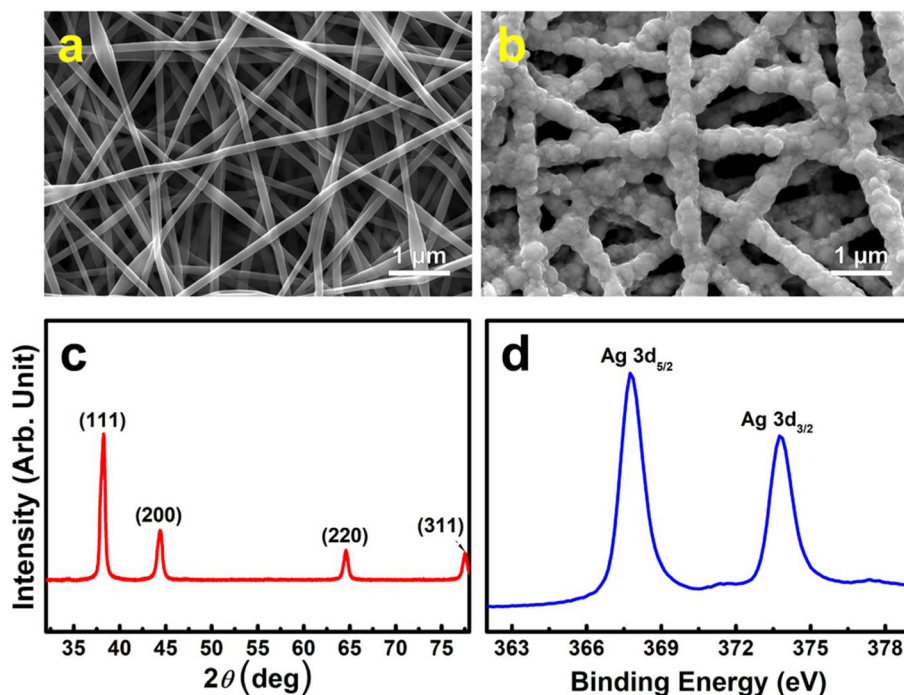


Fig. 2. SEM images of CNF (a) and Ag/CNF (b). XRD pattern (c) and Ag 3d core level XPS spectrum (d) of Ag/CNF SC electrode.

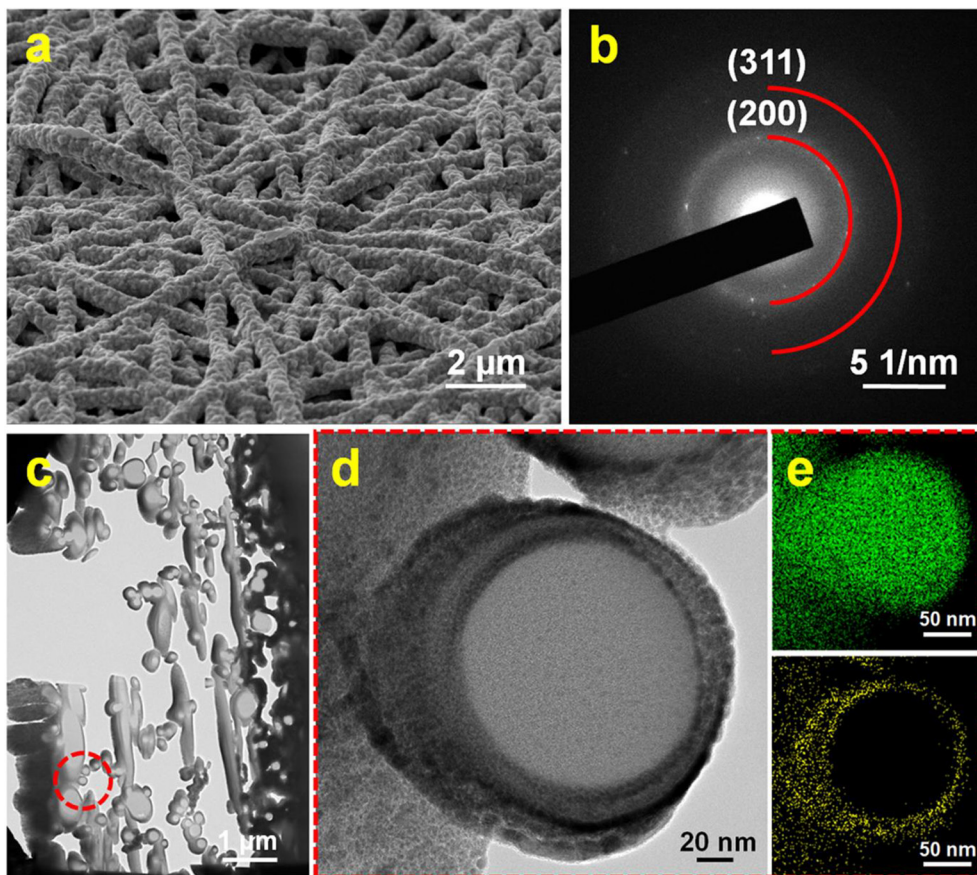


Fig. 3. (a) Surface SEM image of Ag/CNF used for FIB. (b) SAED pattern of Ag in Ag/CNF. Cross-sectional TEM image of Ag/CNF (c) low magnification and (d) high magnification. (e) Elemental mapping of Ag/CNF; green dots (top) represent C and yellow dots (bottom) are Ag. (For interpretation of the references to colour in this figure legend, the reader is referred to the web version of this article.)

Interestingly, with an increase in the molarity of the KOH electrolyte, the reaction kinetics of the electrode were enhanced. As shown in Fig. 4a–c, the peak current output for the anodic and cathodic curves, as well as the area under the curve, increased with increasing scan rate during the CV measurements. The narrow CV curves obtained for the

electrode prepared with 4M KOH may be due to the insufficient availability of K^+ at the surface for the electrochemical reactions. Additionally, the supercapacitor symmetric cell showed an abrupt rise in the current as the anodic potential increased to 0.45 V and beyond, followed by a gradual decrease during the fall in the cathodic potential.

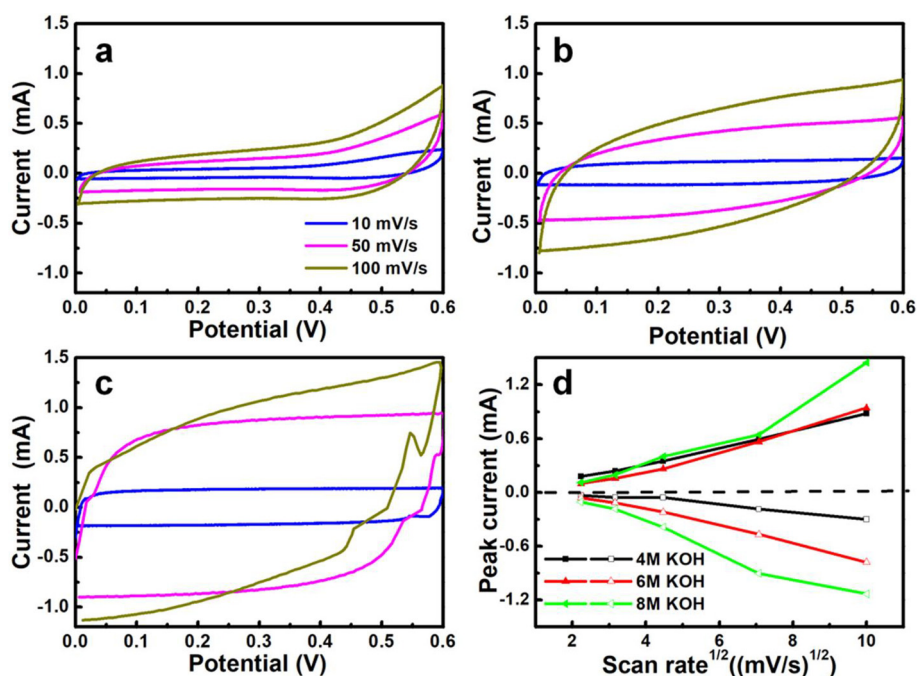


Fig. 4. CV curves of Ag/CNF symmetric SC prepared with aqueous KOH electrolyte at concentrations of (a) 4M, (b) 6M, and (c) 8M, acquired at different scan rates. (d) Corresponding anodic and cathodic peak current vs. square root of scan rate.

The rise in the current could be due to the dissolution of Ag as suggested by Lee et al. [34]. However, the extent of dissolution for sample seems to be small, as the retention for each sample was nearly 100%. Moreover, CNF in the core region may compensate for some minimal dissolution of Ag. Smoother CV curves were obtained with the use of 6M KOH (Fig. 4b) compared to the other two cases studied here. Furthermore, when 8M KOH was used with the electrode, the reaction showed spikes at a lower voltage in the anodic curve due to reduction. Similar spikes were observed for the cathodic peak at higher voltage, which may be due to the oxidation of Ag. Fig. 4d presents the peak anodic and cathodic current for different scan rates. The tests using 4M and 8M KOH gave asymmetric curves, suggesting that some side reactions other than those contributing to the EDLC may be occurring during the anodic cyclic voltammetry measurements with slower kinetics during the cathodic cycle. However, the plots of the anodic and cathodic peak currents as a function of the square root of the scan rate were nearly symmetrical for the electrodes with 6M KOH. Thus, the electrode with 6M KOH provided a controlled redox reaction and balanced diffusion of K^+ during the electrochemical reactions.

The electrolyte plays an essential and vital role in influencing the electrochemical performance of the supercapacitor. Furthermore, the use of KOH as an electrolyte is beneficial due to the high ionic conductivity of K^+ and the fast mobility of the OH^- anions in aqueous solution. Additionally, because the KOH electrolyte is aqueous, it is cost-effective compared to organic electrolytes [35]. K^+ and OH^- have high ionic conductance of 63.6 and 198 ($\text{mho}\cdot\text{cm}^{-2}$), respectively, as documented in Lange's Handbook of Chemistry [36]. Moreover, the ionic radii of hydrated K^+ and OH^- were reported to be 3.31 and 3.00 Å, respectively [36]. For the alternative aqueous electrolyte, Na_2SO_4 , the ionic radius of hydrated Na^+ is 3.58 Å and that of SO_4^{2-} is 3.79 Å. Thus, while exploiting the low cost of the aqueous electrolyte (KOH with different molarities), current densities of 0.1, 0.15, 0.2, 0.3, and 0.5 $\text{mA}\cdot\text{cm}^{-2}$ were achieved during galvanostatic discharge cycling of the Ag/CNFs, as shown in Fig. 5. In all cases, the voltage declined linearly during discharging of the electrode, suggesting excellent electrochemical stability of the supercapacitor electrode. This linear voltage fall is consistent with the ideal capacitor characteristics attributed to the CNF and noble metal, both of which provide EDLC [13]. The

discharge time increased as the concentration of the KOH electrolyte increased. The electrochemical stability of the electrodes is well supported by the high capacitance retention ($\sim 100\%$) demonstrated during long-term cycling for 10,000 cycles. The SEM image in Fig. S4a shows minimal changes in the Ag/CNF electrode morphology after cycling. One of the electrodes from the supercapacitor symmetric cell was used for this morphology analysis. The electrode selected for SEM analysis was first tested for 10,000 galvanostatic charge and discharge cycles. Furthermore, the XRD pattern (see Fig. S4b) of the electrode that underwent severe electrochemical performance testing shows dominant peaks of Ag as indicated by '*' and very weak peaks of Ag_2O_3 appearing at $2\theta = 37.4, 43.7$ and 47.3° indicated by '#'. This result confirms that the oxidation of the electrode is negligible, which is consistent with the observed excellent long-term stability of the electrode [37]. Thus, we established that the Ag/CNF suffer minimal corrosion when incorporated into the electrode, which is a major concern for achieving stable electrochemical performance with an aqueous electrolyte.

In order to double the potential window of the supercapacitor cell to 1.2 V, we prepared an asymmetric SC using dissimilar electrodes, i.e., the carbon nanofibers and the Ag/CNF composite, respectively. Fig. 6a shows the CV plots for the asymmetric supercapacitor in the range of -0.6 to 0.6 V, demonstrating that the curves are much closer to rectangular, suggesting that superior electrochemical double layer capacitance was developed between the dissimilar electrodes. Fig. 6b shows much better symmetry between the anodic and cathodic peak currents when plotted against the square root of the scan rate. The asymmetric supercapacitor offered the advantage of enhanced energy density due to the larger potential window. Additionally, for the asymmetric SC cell, the improved linearity of the anodic and cathodic peak current variation compared to that of the symmetric SC indicates that the anodic and cathodic reactions show the characteristics of a diffusion-controlled process.[38] Given that the CV curves reflect the capacitive characteristics, the electrochemical studies were further extended to galvanostatic measurements in the potential window of 0 to 1.2 V in 6M KOH aqueous electrolyte. The galvanostatic discharge curves (see Fig. 6c) also demonstrated pure capacitor-like behavior, with a linear decrease in the voltage characteristics for all withdrawing current densities and an almost negligible internal resistance (IR) drop.

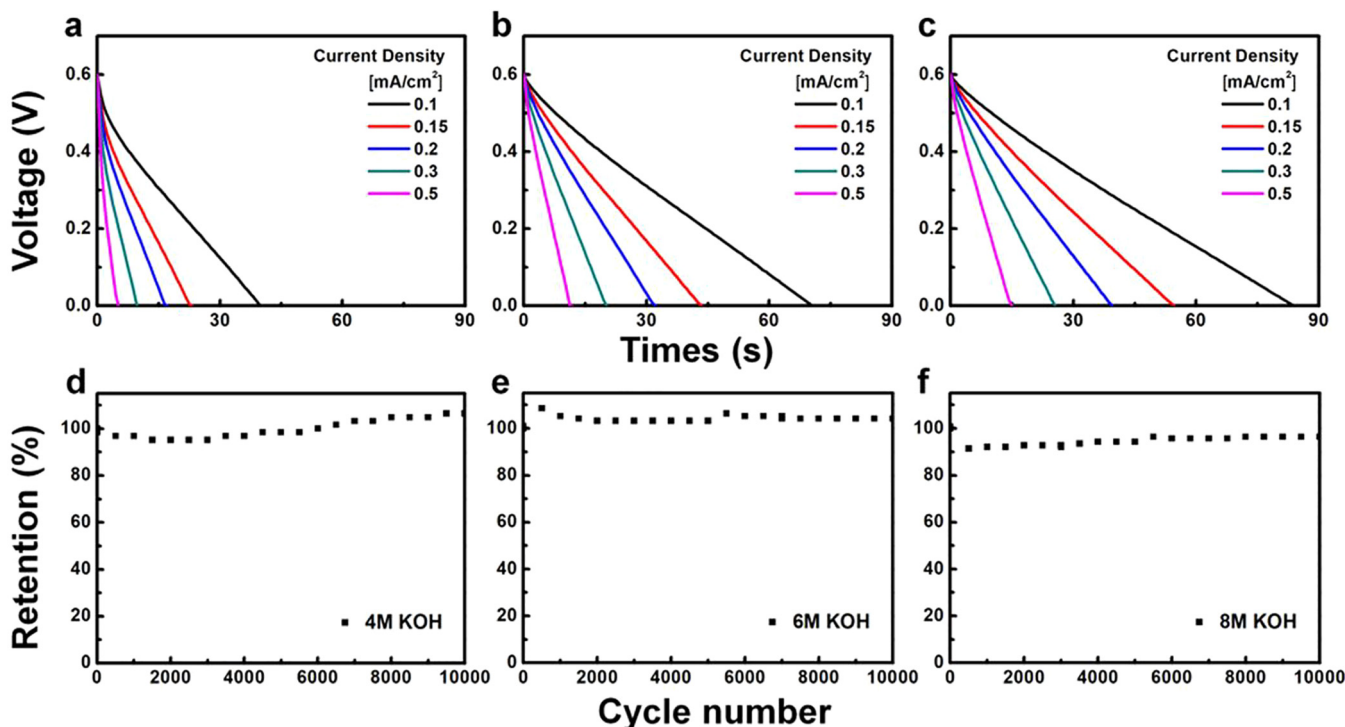


Fig. 5. Ag/CNF symmetric supercapacitors prepared with 4, 6, and 8M aqueous KOH electrolyte; galvanostatic discharge curves acquired at different current densities (a, b, and c), and capacitance retention (%) (d, e, and f).

The asymmetric supercapacitor also showed excellent stability for 10,000 cycles with ~100% capacitance retention, as shown in Fig. 6d.

Fig. 7a demonstrates the variation of the areal capacitances as a function of the electrolyte concentration and current density based on the following equation: [39]

$$C = 2 \frac{I \Delta t}{S \Delta U} \quad (1)$$

where, C is the capacitance of the supercapacitor, S is the total electrode area ($S = 3.08 \text{ cm}^2$), I is the discharge current, Δt is the discharge time, and ΔU is the potential window. The capacitance determined from the galvanostatic charge/discharge measurements is indicative of

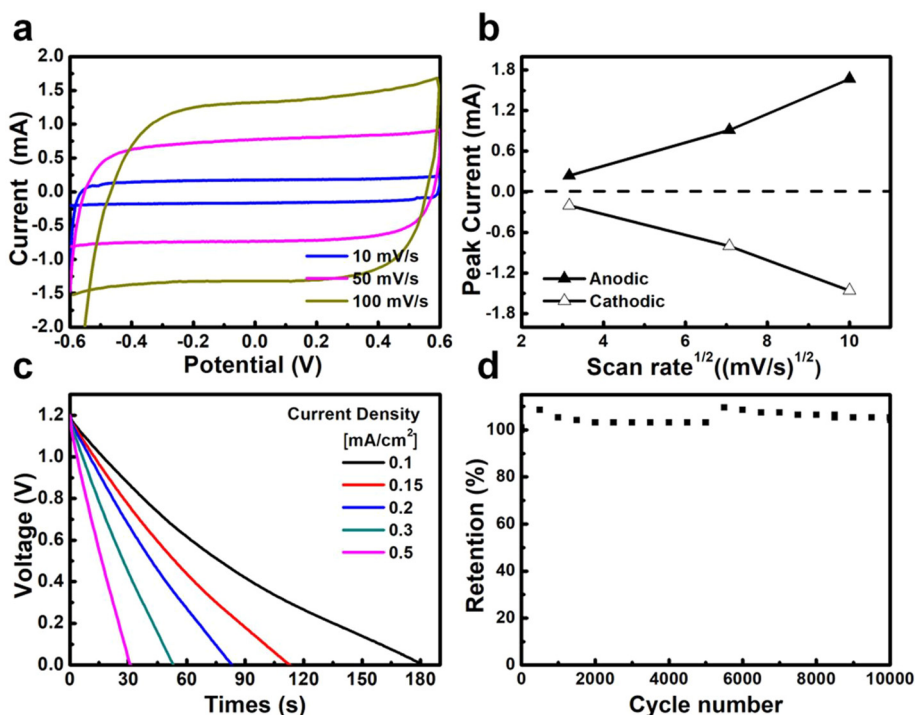


Fig. 6. Electrochemical performance of asymmetric supercapacitor cell (a) CV curves, (b) anodic/cathodic peak current vs. square root of scan rate, (c) galvanostatic discharge curves with variation of the current density, and (d) capacitance retention (%) with 6M KOH aqueous electrolyte.

Table 1
Comparison of specific capacitance obtained in the present study with that of reported Ag-based flexible electrodes for supercapacitors.

Composition	Electrode prepared	Capacitance ($\mu\text{F}/\text{cm}^2$)	Scan rate (mV/s)	Current density ($\mu\text{A}/\text{cm}^2$)	Retention Capacitance (N^{th}) (%)	Potential (V)	Refs.
Ag/CNFs	Nanofibers w/o Binder	30,600	–	100	(10,000) 104	1.2	Present
PANI/Ag/CNF aerogel	Solid electrode	176,000	10	–	–	0.7	[8]
Ag NWs/ WO_3	PET/PDMS substrate	13,600	10	–	(5,000) 72.6	0.5	[9]
Ag/Au/Polypyrrole	Nanowires PET/PDMS substrate	580	–	5.8	(800) 93	0.8	[16]

* Bending cycles.

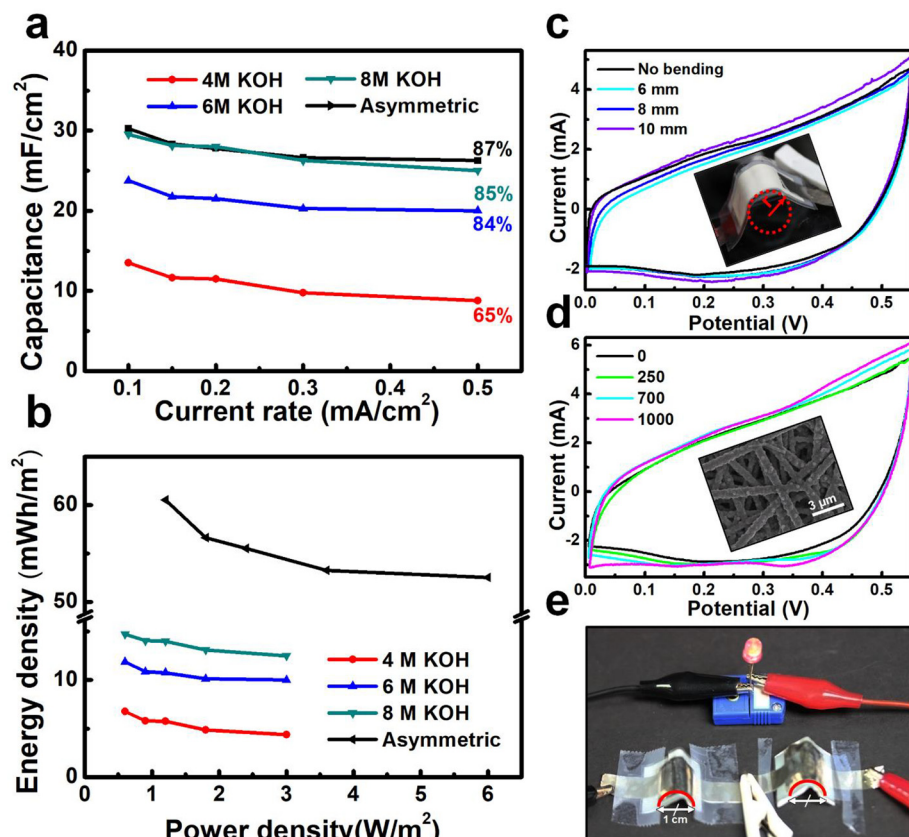


Fig. 7. Electrochemical characteristics of flexible and symmetric/asymmetric supercapacitors: (a) capacitance as a function of current density, (b) Ragone plot (energy density vs. power density). CV curves with varying (c) curvature radii (inset shows bending of Ag/CNF symmetric SC), and (d) number of cycles with bending radius of 8 mm, inset shows SEM image of Ag/CNF after 1,000 bending cycles. (e) Photograph showing bent Ag/CNF SC powering a LED.

excellent current rate capability with almost ideal supercapacitor characteristics as the CNFs and Ag both yield EDLC. As the current density increased, the areal capacitance of each supercapacitor decreased. The decrease in the capacitance could be attributed to the fast kinetic reaction at higher current density, which does not facilitate sufficient diffusion of the electrolyte ions into the electrode. However, at lower current density, the electrolyte ions have sufficient time for adequate diffusion into the electrode, which resulted in higher capacitance. The highest capacitance for the symmetric SC was $29.5 \text{ mF}\cdot\text{cm}^{-2}$ with the use of 8M KOH at a current density of $0.1 \text{ mA}\cdot\text{cm}^{-2}$. The asymmetric SC cell, with a potential window of 1.2 V, demonstrated better rate capacitance, exhibiting 87% capacitance retention when the current density was increased from 0.1 to $0.5 \text{ mA}\cdot\text{cm}^{-2}$. The asymmetric SC cell demonstrated the highest potential value among those summarized in Table 1. Moreover, the retention capacitance of the present SC is superior to that reported for Ag-based flexible electrodes. The rate capability demonstrated by the electrodes in 4M KOH electrolyte was indicative of comparatively poor electrochemical performance, with a decline in the capacitance to 65% of its low current value when the current density was increased from 0.1 to $0.5 \text{ mA}\cdot\text{cm}^{-2}$. The asymmetric supercapacitor with 6M KOH electrolyte exhibited superior current rate capability with higher

capacitance retention ($\sim 87\%$) when the current density was increased gradually. The asymmetric SC exhibited steady performance in the potential window of 0 to 1.2 V during the cyclic voltammetry and galvanostatic measurements, as presented in Fig. 6a and c, respectively. When the symmetric supercapacitor was employed under galvanostatic conditions with 6M and 8M KOH, the capacitance retention was 84 and 85%, respectively, in the potential window of 0 to 0.6 V.

Fig. 7b presents the Ragone plot (energy density versus power density) for the different supercapacitors. The energy densities (E) and power densities (P) were calculated using the following equations: [39]

$$E = \frac{CU^2}{2} \quad (2)$$

$$P = \frac{E}{\Delta t} \quad (3)$$

Here, C is the capacitance of the supercapacitor, U is the potential window used for the galvanostatic measurements, and Δt is the discharge time. The energy density increased from 7 to $15 \text{ mWh}\cdot\text{m}^{-2}$ when the electrolyte was varied from 4M to 8M KOH at a power density of $0.6 \text{ W}\cdot\text{m}^{-2}$, as shown in Fig. 7b, due to the increasing availability of ions. However, the asymmetric SC provided much higher energy densities of 61–53 $\text{mWh}\cdot\text{m}^{-2}$ for power densities varying from 1.2 to

$6 \text{ W}\cdot\text{m}^{-2}$.

The SC was subjected to bending tests and the CV characteristics were assessed while varying the curvature radii, as shown in Fig. 7c. The electrodes were tested initially without bending but later the radius of curvature of the electrode was changed to 6, 8 and 10 mm (Fig. 7c). As the radius of curvature (r) decreased during bending of the SC, the change in the CV curves was negligible. The areal capacitance and long-term performance of the present SC were compared with those of comparable systems reported in the literature (Table 1). The inset of Fig. 7c shows the bent SC marked by the red circle. Further, the electrode was subjected to 1,000 bending cycles ($r = 8 \text{ mm}$ on either side) as shown in Fig. 7d. The inset in Fig. 7d presents an SEM image of the Ag/CNF electrode after 1,000 bending cycles, indicating no damage to the fibers. The resulting CV curves displayed a minor increase in the area under the curve after 1,000 bending cycles, which may be due to more diffusion of the electrolyte ions in the electrode due to strain. However, the shape of the anodic and cathodic curves was similar to that of the pristine SC. As shown in Fig. S5a and c, 1,000 repetitive bending cycles resulted in breaking of CNF at several places. The broken fibers may result in slower charge transfer rate and thereby lower output current and energy density. A region showing damaged fibers after the bending test is highlighted in Fig. S5c. On the other hand, the CNF coated with Ag did not show any breaks, even after 1,000 repetitive bends (Fig. S5b and d). This indicates that the Ag coating contributes to the mechanical stability of CNF. The minimal variation in the CV curves of the SC during the bending test suggests excellent flexibility and mechanical strength of the electrode. The excellent flexibility of the SC electrodes is also demonstrated in Fig. 7e, where the SC was used to power a LED in the bent state.

4. Conclusions

We demonstrated the fabrication of Ag/CNF freestanding electrodes with superior fast electron-transfer channels for symmetric and asymmetric supercapacitor applications. The electrodes exhibited excellent long-term cycling performance with different electrolyte concentrations, with capacitance retention of $\sim 100\%$ after 10,000 charging and discharging cycles. High values of the areal capacitance ($\sim 31 \text{ mF}\cdot\text{cm}^{-2}$), energy density ($61 \text{ mWh}\cdot\text{m}^{-2}$), and power density ($1.2 \text{ W}\cdot\text{m}^{-2}$) were obtained. Moreover, the current rate capability of 87% obtained with a variation of the current density from 0.1 to $0.5 \text{ mA}\cdot\text{cm}^{-2}$ is attributed to the core/shell structure of the highly conductive Ag/CNF composite. Our facile approach that provides a highly flexible Ag/CNF composite with excellent bending capability and negligible fading of the electrochemical response of the electrode holds immense potential for the development of wearable electronic devices and self-powered systems.

Acknowledgment

This research was supported by the Technology Development Program to Solve Climate Changes of the National Research Foundation (NRF) funded by the Ministry of Science, ICT & Future Planning (NRF-2016M1A2A2936760) and NRF-2017R1A2B4005639.

Appendix A. Supplementary data

Supplementary data associated with this article can be found, in the online version, at <https://doi.org/10.1016/j.cej.2018.07.066>.

References

- [1] J. Helmlinger, O. Prymak, K. Loza, M. Gocyla, M. Heggen, M. Epple, *Cryst. Growth Des.* 16 (2016) 3677–3687.
- [2] S. Li, J. Huang, *J. Mater. Chem. A* 3 (2015) 4354–4360.
- [3] Q. Hao, Y. Yu, D. Zhao, C. Xu, *J. Mater. Chem. A* 3 (2015) 15944–15950.
- [4] X. Zang, R. Zhang, Z. Zhen, W. Lai, C. Yang, F. Kang, H. Zhu, *Nano Energy* 40 (2017) 224–232.
- [5] Y. Yan, P. Gu, S. Zheng, M. Zheng, H. Pang, H. Xue, *J. Mater. Chem. A* 4 (2016) 19078–19085.
- [6] W. Cai, Z. Xiong, T. Hussain, J. Yang, Y. Wang, J. Liu, *J. Electrochem. Soc.* 163 (2016) A2515–A2523.
- [7] M. Zhi, C. Xiang, J. Li, M. Li, N. Wu, *Nanoscale* 5 (2013) 72–88.
- [8] X. Zhang, Z. Lin, B. Chen, W. Zhang, S. Sharma, W. Gu, Y. Deng, *J. Power Sources* 246 (2014) 283–289.
- [9] L. Shen, L. Du, S. Tan, Z. Zang, C. Zhao, W. Mai, *Chem. Commun.* 52 (2016) 6296–6299.
- [10] X. Li, S. Ding, X. Xiao, J. Shao, J. Wei, H. Pang, Y. Yu, *J. Mater. Chem. A* 5 (2017) 12774–12781.
- [11] D.S. Patil, S.A. Pawar, R.S. Devan, M.G. Gang, Y.-R. Ma, J.H. Kim, P.S. Patil, *Electrochim. Acta* 105 (2013) 569–577.
- [12] E. Samuel, H.S. Jo, B. Joshi, H.G. Park, Y.I. Kim, S. An, M.T. Swihart, J.M. Yun, K.H. Kim, S.S. Yoon, *Appl. Surf. Sci.* 423 (2017) 210–218.
- [13] Y. Yan, T. Wang, X. Li, H. Pang, H. Xue, *Inorg. Chem. Front.* 4 (2017) 33–51.
- [14] Y. Yan, B. Li, W. Guo, H. Pang, H. Xue, *J. Power Sources* 329 (2016) 148–169.
- [15] S. Zheng, X. Li, B. Yan, Q. Hu, Y. Xu, X. Xiao, H. Xue, H. Pang, *Adv. Energy Mater.* (2017).
- [16] H. Moon, H. Lee, J. Kwon, Y.D. Suh, D.K. Kim, I. Ha, J. Yeo, S. Hong, S.H. Ko, *Sci. Rep.* 7 (2017) 41981.
- [17] L. Tang, F. Duan, M. Chen, *RSC Adv.* 6 (2016) 65012–65019.
- [18] Y. Shao, H. Wang, Q. Zhang, Y. Li, *J. Mater. Chem. C* 1 (2013) 1245–1251.
- [19] D.S. Patil, S.A. Pawar, J.H. Kim, P.S. Patil, J.C. Shin, *Electrochim. Acta* 213 (2016) 680–690.
- [20] D.S. Patil, J. Shaikh, S. Pawar, R. Devan, Y. Ma, A. Moholkar, J. Kim, R. Kalubarme, C. Park, P. Patil, *PCCP* 14 (2012) 11886–11895.
- [21] L. Tang, F. Duan, M. Chen, *J. Mater. Sci.: Mater. Electron.* 28 (2017) 7769–7777.
- [22] B. Pandit, V. Devika, B.R. Sankapal, *J. Alloy. Compd.* 726 (2017) 1295–1303.
- [23] Y. Li, H. Fu, Y. Zhang, Z. Wang, X. Li, *J. Phys. Chem. C* 118 (2014) 6604–6611.
- [24] J. Wu, Z. Li, Y. Lin, *Electrochim. Acta* 56 (2011) 2116–2121.
- [25] J. Huang, H. Wu, D. Cao, G. Wang, *Electrochim. Acta* 75 (2012) 208–212.
- [26] X. Wang, P. Zhang, S. Vongehr, S. Tang, Y. Wang, X. Meng, *RSC Adv.* 5 (2015) 45194–45200.
- [27] M. Xianwen, T.A. Hatton, C.R. Gregory, *Curr. Org. Chem.* 17 (2013) 1390–1401.
- [28] S. An, H.S. Jo, D.Y. Kim, H.J. Lee, B.K. Ju, S.S. Al-Deyab, J.H. Ahn, Y. Qin, M.T. Swihart, A.L. Yarin, *Adv. Mater.* 28 (2016) 7149–7154.
- [29] S. An, B.N. Joshi, M.W. Lee, N.Y. Kim, S.S. Yoon, *Appl. Surf. Sci.* 294 (2014) 24–28.
- [30] A. Sivanesan, E. Witkowska, W. Adamkiewicz, Ł. Dziewit, A. Kamińska, J. Waluk, *Analyst* 139 (2014) 1037–1043.
- [31] C. Pan, Y. Lv, H. Gong, Q. Jiang, S. Miao, J. Liu, *RSC Adv.* 6 (2016) 17415–17422.
- [32] J.K. Gan, Y.S. Lim, N.M. Huang, H.N. Lim, *RSC Adv.* 5 (2015) 75442–75450.
- [33] Y. Yan, H. Xu, W. Guo, Q. Huang, M. Zheng, H. Pang, H. Xue, *Inorg. Chem. Front.* 3 (2016) 791–797.
- [34] H. Lee, S. Hong, J. Lee, Y.D. Suh, J. Kwon, H. Moon, H. Kim, J. Yeo, S.H. Ko, *ACS. Appl. Mater. Interfaces* 8 (2016) 15449–15458.
- [35] C. Zhong, Y. Deng, W. Hu, J. Qiao, L. Zhang, J. Zhang, *Chem. Soc. Rev.* 44 (2015) 7484–7539.
- [36] J.G. Speight, *Lange's Handbook of Chemistry*, McGraw-Hill, New York, 2005.
- [37] G.I. Waterhouse, J.B. Metson, G.A. Bowmaker, *Polyhedron* 26 (2007) 3310–3322.
- [38] R. Kumar, P. Rai, A. Sharma, *RSC Adv.* 6 (2016) 3815–3822.
- [39] P. Yang, W. Mai, *Nano Energy* 8 (2014) 274–290.